Journal of Alloys and Compounds 1021 (2025) 179643

Contents lists available at ScienceDirect

Journal of Alloys and Compounds

journal homepage: www.elsevier.com/locate/jalcom

Process development and application of hot forging arc-based additive manufacturing on Haynes® 282 for microstructural and mechanical improvements

Igor Oliveira Felice [a,*], Pedro Rodrigues Marçal [b], Jiajia Shen [b], Luis Fernando Ladinos Pizano [c], Wei Xiong [c], Norbert Schell [d], Telmo Gomes Santos [a,e], João Pedro Oliveira [b]

[a] *UNIDEMI, Department of Mechanical and Industrial Engineering, NOVA School of Science and Technology, Universidade NOVA de Lisboa, Caparica 2829-516, Portugal*
[b] *CENIMAT/I3N, Department of Materials Science, NOVA School of Science and Technology, Universidade NOVA de Lisboa, Caparica 2829-516, Portugal*
[c] *Physical Metallurgy and Materials Design Laboratory, Department of Mechanical Engineering and Materials Science, University of Pittsburgh, Pittsburgh, PA, USA*
[d] *Helmholtz-Zentrum Hereon, Institute of Materials Physics, Max-Planck-Str. 1, Geesthacht 21502, Germany*
[e] *Laboratório Associado de Sistemas Inteligentes, LASI, Guimarães 4800-058, Portugal*

ARTICLE INFO

Keywords:
Arc-based additive manufacturing
Hot forging
Haynes® 282
Grain refinement
Mechanical strength

ABSTRACT

Haynes® 282, a nickel-based superalloy, is renowned for its exceptional strength, thermal stability, and resistance to oxidation and creep. While directed energy deposition arc-based additive manufacturing of this alloy has been explored, the formation of large columnar grains and high texture leading to anisotropy and suboptimal mechanical performance remains a significant challenge. This study introduces an interlayer in-situ mechanical deformation approach, known as hot forging, to address these issues. The hot forging process, applied at high temperatures, aims to refine grain structure, reduce porosity, and enhance mechanical properties. The dynamic analysis of the process using a high-speed camera imaging allowed to calculate a forging force exceeding 1000 N. Two single-bead multi-layered walls were fabricated, one with hot forging and one without. Results demonstrated a 22 % reduction in porosity upon hot forging. Electron backscatter diffraction analysis indicated that the hot forged sample has less texture, and the average grain size decreased from 1746 to 1262 μm and from 1053 to 696 μm in the top and middle wall regions, respectively. Synchrotron X-ray diffraction revealed a small variation in phase composition and confirmed that hot forging promotes refined grain structures with less texture. The ultimate tensile strength in the horizontal direction improved by 8 % with hot forging, while elongation decreased by 30 %. Electrical conductivity and microhardness measurements were similar for both processes. The findings confirm the efficacy of in-situ hot forging in enhancing microstructure and mechanical performance, highlighting its potential for high-cost and low-machinability materials in arc-based additive manufacturing.

1. Introduction

Arc-based additive manufacturing (AM) is intricately connected to Industry 4.0 due to its reliance on advanced technologies which are fundamental to the fourth industrial revolution. Recognized as a superior rapid prototyping method for producing near-net-shape and complex geometries with higher material efficiency and lower production time [1], several key points underscore the relationship between this process and Industry 4.0, namely automation and robotics, Internet of Things (IoT), advanced materials processing, and reduction of material losses [2]. Arc-based Directed Energy Deposition (DED) is an AM technology, and involves multiple pass depositions using established welding techniques, which makes the initial setup straightforward due to equipment low costs and versatility [3–5]. Nonetheless, the process faces challenges related to material's applicability (as some materials exhibit low weldability) and the thermal nature of the process (sequential thermal cycles and significant heat accumulation) that results in anisotropic metallurgical, electrical, and mechanical properties, among other complexities [6–9].

Strategies and advancements have been developed to enhance thermal management in arc-based DED processes, addressing issues such as heat accumulation, thermal stresses, and resultant anisotropic

---

[*] Corresponding author.
E-mail address: i.felice@campus.fct.unl.pt (I.O. Felice).

https://doi.org/10.1016/j.jallcom.2025.179643
Received 18 October 2024; Received in revised form 13 February 2025; Accepted 6 March 2025

properties. Key approaches include the control of heat input through the adjustment of welding parameters (such as wire feed speed, current, voltage, and travel speed) [10,11], interpass cooling (implementing controlled cooling periods between deposition passes) [12], active cooling techniques (utilizing external cooling systems) [6], thermal modeling and simulation, and real-time temperature monitoring [13,14]. Effective thermal management is critical in arc-based additive manufacturing, as it significantly influences the formation and growth of columnar grains. By adjusting the thermal history, it is possible to control the microstructure and improve the mechanical properties of the produced components [15].

In addition to thermal control, mechanical deformation applied during or after the deposition process has shown promise in refining columnar grains and transitioning them toward equiaxed structures [16]. For example, techniques such as rolling or peening nucleation sites and breaking down the elongated grain structure. In-process rolling applied to each layer could significantly reduce the β grain size in Ti-6Al-4V alloys with minimal deformation [17]. McAndrew et al. [18] demonstrated that using rollers with large radius increases the recrystallized area extent, resulting in a more uniform grain size, while higher loads further enhance post-rolling refinement. Marinelli et al. [19] observed that random texture formation after rolling a tantalum linear structure led to isotropic mechanical properties, as the deformed layer undergoes recrystallization during subsequent deposition, developing new strain-free equiaxed grains. Hammer peening has also proven effective for grain refinement and texture reduction in relatively thick sections, particularly in Ti-6Al-4V alloys, where even minimal plastic deformations improve mechanical properties [20,21]. Ultrasonic impact treatment involves applying high-frequency ultrasonic vibrations to the deposited layers, causing localized plastic deformation. This technique can refine the microstructure by breaking up columnar grains and encouraging equiaxed grain growth. It has been effective for stainless steels, nickel-based alloys, and aluminum alloys, significantly reducing porosity in the latter [22–24]. Post-deposition forging at high temperatures can also reduce columnar grain structures by promoting recrystallization and grain growth into more equiaxed forms. During mechanical deformation, particularly at elevated temperatures, dynamic recrystallization can occur, leading to the formation of new, strain-free grains within the deformed microstructure, thus transforming columnar grains into finer, equiaxed grains. This process also disrupts the continuity of columnar grain boundaries, creating high-angle grain boundaries that act as nucleation sites for new grains [25]. Furthermore, post-heat treatments or the heat from subsequent deposited layers can induce static recrystallization in arc-based AM, where new grains form without external stress. This further refines the grain structure and reduces the prevalence of columnar grains [26].

In the context of discontinuous hot deformation, Xu et al. [27] utilized a compact high-dynamic actuator as an integrated hammering power source, enabling the generation of substantial hammering force at relatively high frequencies. This technique effectively minimized shrinking holes and closed pores, while enhancing microhardness and compressive yield strength. Ma et al. [28] introduced a compound arc and vibration shock forging-rolling (CAVSFR) method, which reduced the average grain size of low carbon steels from 9.6 μm (using conventional arc-based AM) to 6.4 μm. The grain refinement was attributed to the combined effects of static-force rolling, vibration-shock forging, and micro self-forging within the molten pool. Fu et al. [29] explored the hot deformation behavior of TC4-DT titanium alloy fabricated via wire and arc additive manufacturing (WAAM) with in-situ forging. This approach facilitated the formation of macrostructures comprising fully equiaxed prior-β grains, while preserving isotropy in mechanical properties. Also, for Ti-based alloys, Maurya et al. [30] employed a hybrid method combining WAAM with a single-step hot forging process. The resulting microstructures revealed an instability region at high strain rates and lower temperatures, associated with flow localization and lamellae kinking. Conversely, high-efficiency and stable regions were linked to dynamic recrystallization within the temperature range of 900–950 °C at strain rates below 1 s^{-1}. Forged samples at 920 °C and strains of 0.6, 0.8, and 0.9 exhibited superior strength, elongation, and reduced texture compared to as-received and stress-relieved samples. An innovative in-situ forging adapted torch system was developed for arc-based AM using a crown hammer to promote grain refinement and pore collapse, featuring a system with path freedom that minimizes the distance between the hammer actuator and the wire, thereby simplifying the system's volume and complexity [31–34]. This technology proved effective for various materials, enhancing mechanical properties and reducing anisotropy. However, a significant challenge remains in adjusting the distance between the hammer actuator and the wire, as different material compositions and welding conditions result in varying molten pool dynamics and thermomechanical behaviors.

Haynes® 282, a high-performance nickel-based superalloy, has not yet been tested in additive manufacturing (AM) using the in-situ hot forging mechanism. This alloy is known for its exceptional weldability and fabricability, surpassing other wrought alloys with comparable creep strength. Despite its high strength at temperatures up to 900 °C, Haynes® 282 demonstrates remarkable formability, fabricability, and forgeability. Its superior weldability, compared to other γ'-strengthened alloys, is attributed to its enhanced resistance to strain-age cracking, making it a prime candidate for advanced ultra-supercritical steam applications, including turbines and other critical components [35]. Current research has shown that Haynes® 282 exhibits excellent resistance to solidification cracking, outperforming the commonly welded 718 alloy. Furthermore, the alloy demonstrates superior strain-age cracking resistance, highlighting its potential for both welding and advanced manufacturing techniques. [36,37]. However, arc-based AM processes for this material often result in a characteristic columnar grain morphology due to directional heat extraction [38,39]. Pizano et al. (2024) reported that during layer overlap, columnar grains underwent epitaxial growth atop preceding grains. This competitive growth mechanism filtered out preferential crystallographic orientations, leading to significant increases in grain size and texture with each successive layer. These changes compromised mechanical performance and increased anisotropy [40].

Given these findings, Haynes® 282 presents significant potential for further investigation in advanced manufacturing, particularly in addressing the challenges related to columnar grain formation in arc-based AM processes. This study was conducted to understand the effects of in-situ hot forging as a mechanical deformation technique for grain refinement. Thermal management was also employed to mitigate the deleterious effects of excessive heat input, with the molten pool dimensions measured to design the optimal distance between the hammer actuator (or deformation region) and the wire. The as-built materials were characterized using advanced microstructural and mechanical evaluation techniques. The results confirm the potential of hot forging technology for enhancing the performance of this high-application material.

2. Materials and methods

2.1. Materials and experimental procedure

The as-received Haynes® 282 was obtained in the form of a 1.1 mm diameter wire and the chemical composition (in wt%) can be found in Table 1. The setup used to produce the walls consisted of an adapted arc-based DED torch mounted to a moving 3-axes head within a working envelope of 2760 × 1960 × 2000 mm. A *Oerlikon Citowave III 520* was used as the process power source. Table 2 summarizes the main deposition parameters, which were optimized considering single beads previously tested. The wire was deposited on an ASTM A36 carbon steel plate (80 × 10 × 200 mm) to build 2 multi-layered and single-bead walls, using hot forging (HF) and conventional (CO) arc-based DED processes. To prevent the melt pool contamination, both substrates had

Table 1
As-received Haynes® 282 wt composition.

Element	Ni	Cr	Co	Mo	Ti	Al	Fe	Mn	Si	C	B
Weight (%)	Balance	20	10	8.5	2.1	1.5	1.5 max.	0.3 max.	0.15	0.06	0.005

Table 2
Detailed deposition parameters for Haynes® 282.

Welding mode	GMAW – Synergic mode DC +
Wire feed speed	4.2 m/min
Travel speed	330 mm/min
Approximate voltage	17.4 V
Contact tip to work distance	10 mm
Shielding gas	Argon & Helium
Gas flow rate	19 L/min
Interpass Temperature	85 °C – 95 °C
Forging Pressure	4 bar
Forging Frequency	8 Hz

to be roughed with an angle grinder. The length of the wall was defined as 160 mm and a 2-minute dwell time was set, so that each subsequent deposition started when the previously deposited layer reached a temperature below 100 °C, avoiding distortions and defects caused by high heat accumulation associated to WAAM [6]. Depositions were continuously performed until the wall reached a height of 58 mm. This value was defined considering a specimen arrangement for later microstructural and mechanical characterization.

The forging pressure was adjusted to 4 bar using a manual pressure regulator valve coupled to the forging system, with an operational range of 0–10 bar. This pressure value was selected based on preliminary tests that evaluated the effects of various forging pressures on material deformation. Pressures below 4 bar resulted in insufficient forging, while pressures above 4 bar led to unstable process characterized by uncontrolled spattering and undesirable system vibrations. The forging frequency was established at 8 Hz, guided by prior studies [31,32] that considered the system integrity and process duty cycle and travel speed. The duty cycle and forging frequency can be adjusted depending on the travel speed. Additionally, the forging pressure must be optimized for each material as variations in alloy composition result in distinct mechanical, thermal, and microstructural properties.

To ensure and evaluate the microstructural homogeneity of the deposited material, electrical conductivity measurements were performed on the cross-section samples of both HF and CO walls. These samples were sliced from the as-built walls in region of deposition stability using an industrial saw machine and embedded. This electrical property, when evaluated on thermomechanically processed materials, can be related to microstructural features and presence of subsuperficial defects, namely cracks, pores, and lack of fusion [41]. For this reason, Four-Point Direct-Current Potential Drop Measurement technique were used to measure the electrical conductivity. A Jandel™ four-point probe with 0.635 mm probe spacing and 40 µm probe tip radius was used together with a Keithley™ 2450 Source Measurement Unit (SMU), imposing an intensity of 79 mA between the external points. Moreover, also to evaluate the presence of internal defects (pores, lack of fusion, voids), the volume of voids (VV) was calculated via gravimetry technique, which is a simple and cost-effective method that provides reliable results for internal porosity [42]. The mass of the samples was measured in ambient air and fully immersed in acetone (apparent mass). With these measurements, the density of the material (ρ) could be calculated by Eq. 1, where ρ_{liq} represents the density of acetone (7.96×10^5 kg/m^3), m_{air} and m_{liq} denotes the mass measured in air and while submerged in acetone respectively. The void volume percentage was calculated using Eq. 2 by comparing the density of the samples (ρ_{sample}) to a benchmark density (ρ_{ref} – in this study, corresponds to the wire feedstock material density calculated by the same methodology).

$$\rho = \quad \rho_{liq}.m_{air} / (m_{air} - m_{liq}) \tag{1}$$

$$VV = \quad (\rho_{ref} - \rho_{sample}) / \rho_{ref} \tag{2}$$

2.2. Hot forging process design and dynamic characterization

The hot forging process consists of a metal 3D printer prototype based on Gas Metal Arc Welding (GMAW) principle with an adapted torch with a symmetrically pneumatic system, ensuring consistent force generation without imbalances, that actuates a crowned hammer tip, forging the material immediately after its deposition. The forging force (F_F), forging frequency (F_f), distance to arc centre (DAC), duty cycle (%), forging step (F_S) are the main process parameters that may influence the material deposition, including its microstructural features and mechanical properties as well as final geometrical shape. A detailed description of the process development is presented in Ref. [31] and a schematic illustration of the in-situ hot forging torch is depicted in Fig. 1. In this study, the hammer's design, which governs the DAC parameter, was developed considering the videos recorded using a Photron FASTCAM Mini WX50 high-speed camera, which operates at a frame rate of 1000 frames per second with 1280 × 800 pixels resolution. The camera was paired with a Nikon AF NIKKOR 28–105 mm macro lens and a longpass filter with cut-on wavelength of 800 nm, allowing precise observation of the melting pool and impact point. The objective was to measure the molten pool size for different layers along the vertical deposition of pre-deposition trials, when certain specific set of parameters was used. Thus, based on these measurements, the hammer crown was designed to ensure that the contact between the hammer surface and the deposited material occurred within a viscoplastic region, i.e., between the molten pool (liquid) and the solidified material. For measurements, the wire feedstock was used for calibration. The camera was also used to detect any potential issues during the deposition process. to monitor potential issues during the deposition process. The video data, combined with other parameters such as current, voltage, and temperature, provides a comprehensive understanding of the arc-based process [43].

The dynamic characterization of the HF process was conducted using the same high speed camera setup. The purpose was to assess the forging force and stress imposed to the deposited material by analyzing the physical behavior of the hammer during forging. The video of the instant of impact was divided into frames and the hammer position on a 2-D plane could be registered for each image. Thus, the hammer vertical movement over time was graphically analyzed, as presented in Fig. 2, and the hammer velocity (v_f) before the impact was calculated allowing to estimate the impact time (δt). Finally, the forging force (F_F) could be approximated using the principles of impulse and momentum, as outlined in Eq. 3, following the methodology defined in [31]. The quantity I [N·s] represents the impulse, Q [kg·m/s] denotes the linear momentum, m [kg] is the mass of the moving hammer parts, Δv [m/s] indicates the difference between initial and final velocities of the forging hammer, F_F [N] stands for the average force exerted during the impact (forging), and δt [s] reflects the duration of the impact. As the initial velocity of the hammer is considered to be null, Δv is assumed to be the final velocity (v_f). Also, the stress imposed to the material can be assessed considering the estimated forging force and the contact area. The area formed during each hammer strike is contingent upon both the bottom surface of the hammer and the forging step, denoted as Fs, which represents the distance traveled by the hammer in a single cycle. The calculation steps and equations are presented by Duarte et al., (2022) [31]. The forged area

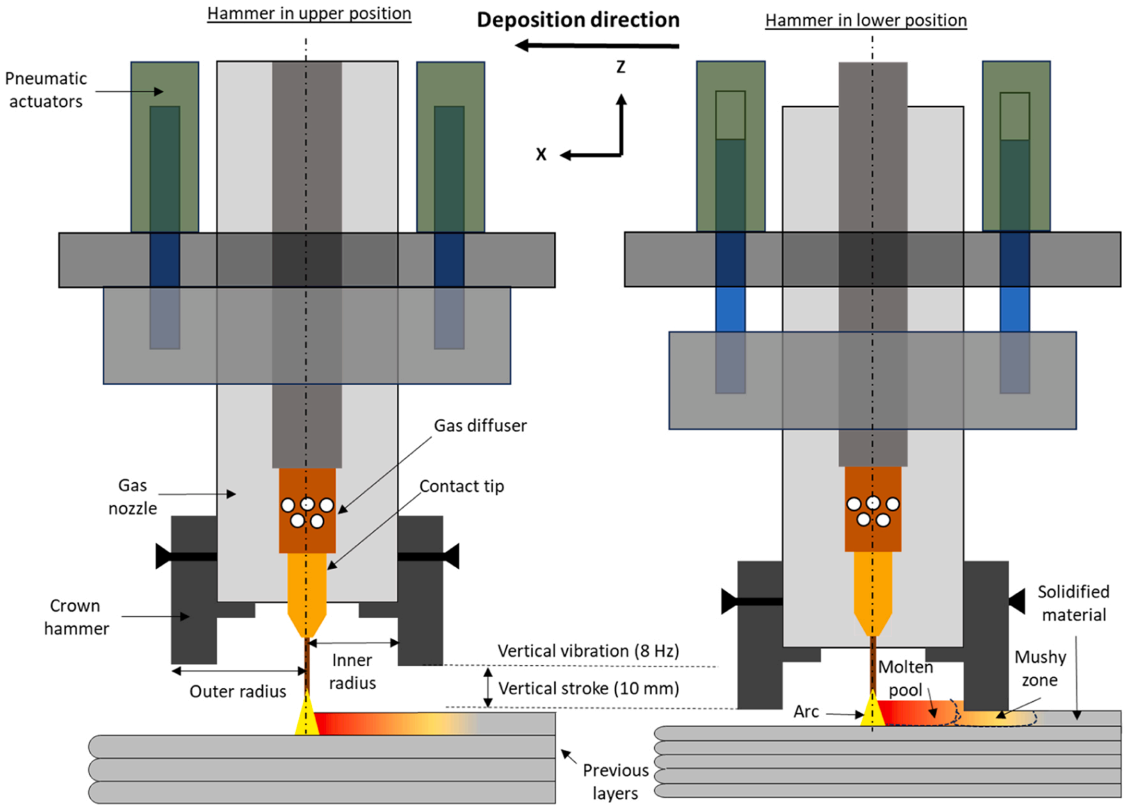

Fig. 1. Schematic illustration of the in-situ hot forging and process dynamics.

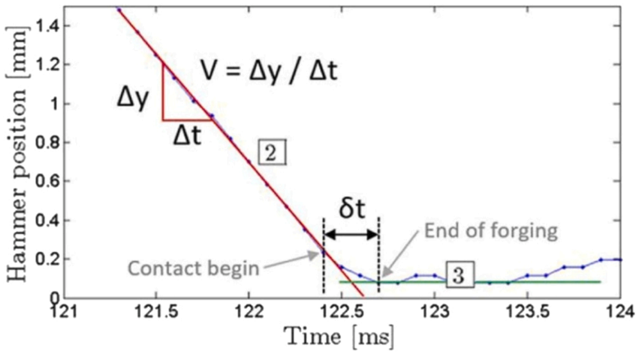

Fig. 2. Hammer position over time during deposition, highlighting the moment of forging and the impact time (δt). Region 2 represents a constant velocity region and 3 is the reminiscent forging [31].

remains constant throughout the process as the hammer's geometrical characteristics and deposition parameters, such as travel speed and forging frequency, are maintained constant.

$$I = \quad \Delta Q = m\Delta v = F_F.\delta t \tag{3}$$

2.3. Microstructural and mechanical characterization

The cross sections extracted from the Haynes®282 walls for electrical conductivity measurements were also used for microstructural characterization. An *Olympus CX40* inverted optical microscope (OM) was used to assess the microscopic features of samples manufactured by HF and CO arc-based processes. The cross-sectional specimens were embedded, grinded until the grit P 4000, polished using 3 microns diamond paste and etched by swabbing the material for 200 seconds with the Kalling's N° 2 reagent. The texture and grain size were evaluated through electron backscatter diffraction (EBSD) using an FEI Apreo Scanning Electron Microscope (SEM) equipped with an EDAX Hikari EBSD detector. The EBSD patterns were indexed using the Ni-rich FCC matrix, and the grain size was estimated considering the average circular equivalent diameter. Synchrotron X-ray diffraction (SXRD) was used as part of the microstructural characterization. Measurements were performed at the P07 beamline of the High Energy Materials Science (HEMS), PETRA III/DESY, using a wavelength of 0.1423 Å and an incident beam of 0.5 × 0.5 mm. A Perkin-Elmer detector was used to acquire the 2D Debbye-Scherrer diffraction rings and qualitative information on the grain size, texture and orientation of the analyzed material was captured on the central region of the wall cross-section for the two samples (HF and CO). LaB_6 powder was used for calibration.

Microhardness measurements performed using a *Mitutoyo HM-112 Micro-Vickers Hardness Testing Machine*, with a load of 1.0 kgf (HV1.0) and indentation time of 10 s were used to create a hardness heatmap to evaluate the uniformity within the as-built materials. A vertical distance of 500 µm between 2 consecutive indentations was used to avoid any interference between consecutive measurements [44]. Regarding the mechanical characterization, specimens for tensile test were extracted from HF and CO walls after lateral milling of the as-built parts using electro-discharge machining (EDM). Samples were extracted in horizontal and vertical directions. Tensile tests were performed using a *Shimadzu AG-50kNG* Universal Mechanical Testing Machine with a constant displacement of 0.03 mm/s.

3. Results and discussion

The hammer design was developed using images from high-speed videos recorded during pre-deposition trials. Using the deposition parameters presented in Table 1, a preliminary single-bead multi-layered wall was fabricated, and the respective molten pool size was measured over different layers. For the measurements, the welding wire was used for calibration and the measurements are presented in Fig. 3 – for

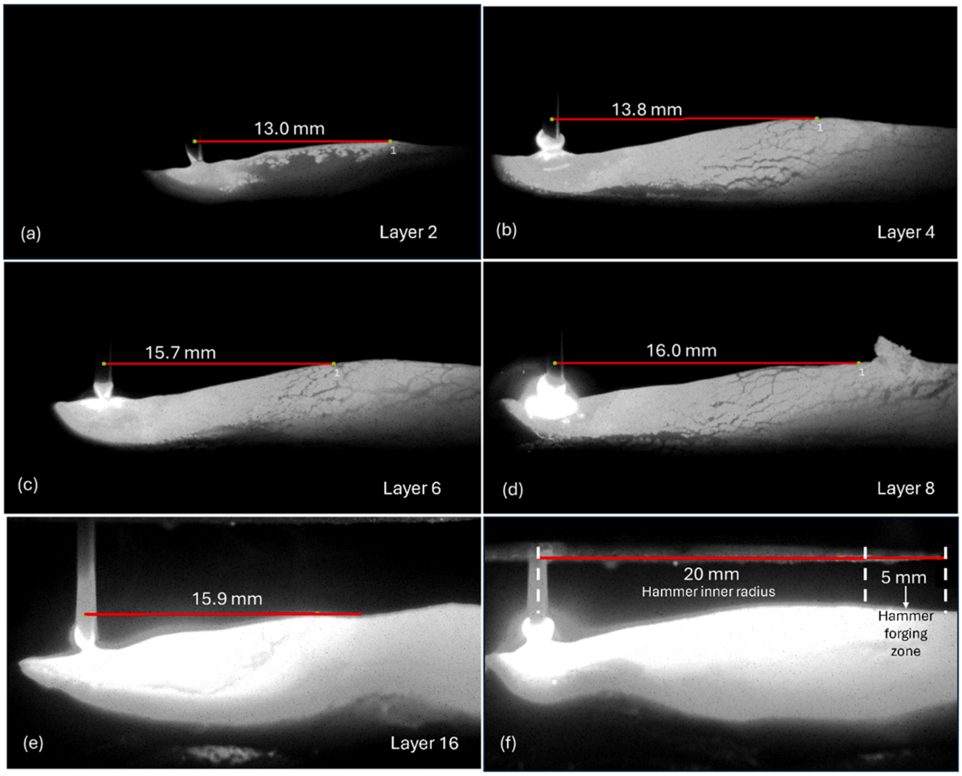

Fig. 3. Illustration of the molten pool and its measured length along different layers (a-e), and representation of the hammer fundamental design dimensions. The red line depicts the molten pool length measured from the welding wire.

different layers. In continuous depositions with no thermal control, it is expected a higher heat accumulation on the upper-deposited layers comparing to the bottom ones, leading to larger molten pools for these layers on the top of the walls [6]. However, the interpass time was employed to allow heat dissipation and reduce the material surface temperature below 100 °C before starting a new layer deposition. This approach, also known as passive natural cooling, was sufficient to maintain the molten pool size approximately constant after the 8th layer, where a maximum length of 16.0 mm was observed. Hence, a forging hammer designed with 20 mm of inner radius was considered convenient for this deposition set of parameters as the impact would always occur in a region in the weld pool where the material is partially solid and partially liquid (mushy zone). The 20 mm hammer inner radius and the 5 mm forging zone/surface are highlighted in Fig. 3(f). It is essential to emphasize that the assessment of the molten pool size is required for each distinct material tested, as well as for varying parameter sets, even when using the same material. Variations in wire feed speed and travel speed result in different heat inputs, which significantly affect the molten pool dynamics and geometry. Recent studies have employed numerical simulations to analyze the behavior of the molten pool shape [45–47]. However, due to the complexity and low repeatability of welding processes, in situ monitoring using high-speed and/or thermal cameras has proven to be an effective solution.

For the forging dynamic evaluation, it is feasible to propose that the vertical motion of the hammer initiates from a zero-velocity state, undergoes acceleration at a defined rate, and achieves a constant velocity just before the impact moment. This behavior can be discerned through the hammer bottom surface temporal position depicted in Fig. 4, where the typical linear displacement is noted before the impact. Fig. 5 presents a sequence of frames of the hammer vertical movement, starting from the upper position (Fig. 5-a) to the lowest position (Fig. 5-f) through series of sequential intermediate points, depicted in Figs. 5-b to 5-e. In total, more than 50 frames are taken into consideration for measurements surrounding the impact moment, with one repetition of the measurements to guarantee repeatability. Derived from linear regression, the final velocity before the impact, v_f, and the impact time, δt, were determined to be approximately 0.85 m/s and 0.5625 ms, respectively. Considering a mass of 0.675 kg for the moving components of the torch, the approximate instantaneous force due to impact applied to the material during forging was calculated to be 1022 N. The forging step was measured to be 0.6875 mm, with the average width of the hot forged sample being 6.23 mm. Consequently, the calculated average area forged in each hammer stroke is 4.28 mm^2, and the estimated

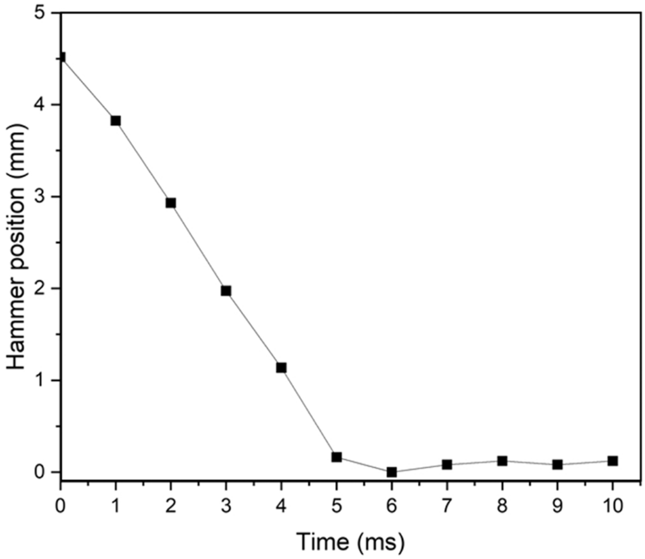

Fig. 4. Hammer position over time during deposition of Haynes®282 with HF process.

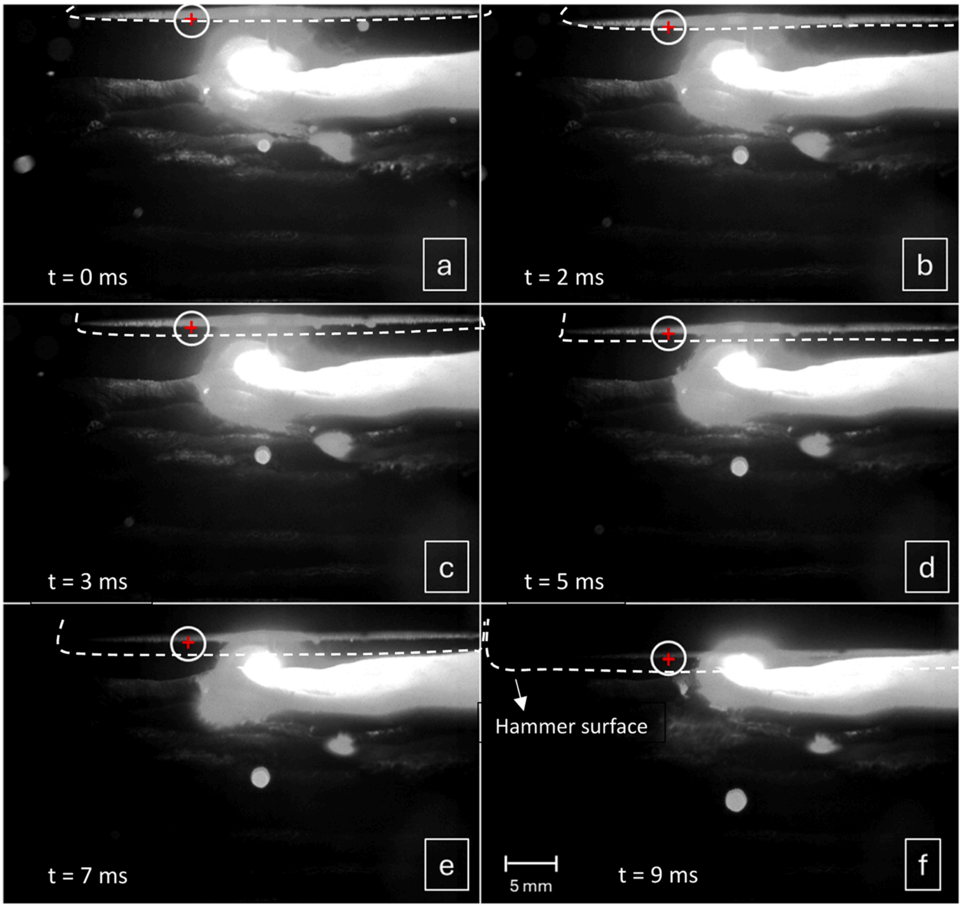

Fig. 5. Sequence of frames illustrating the hammer vertical movement from upper (a) to lower (f) positions, pointing the hammer bottom surface with a red cross. The dashed line depicts the hammer surface.

pressure is approximately 239 MPa. It is advisable to measure and control the material's temperature during impact, as the forging dynamics can fluctuate even with minor temperature variations.

An immediate consequence of the forging process is the collapse and/or reduction of the material's internal voids (delamination, pores, and cracks if eventually formed). Considered one of the significant defects in Ni-based superalloys, particularly relevant to manufacturing processes with high cooling rates, such as in WAAM [48], the volume of internal voids (VV) was evaluated, revealing that the HF process resulted in a 22 % reduction in VV compared to the conventional process. Despite conventional WAAM exhibited a reasonable and low level of voids (1.09 %), forging achieved even lower levels (0.89 %), consistent with findings in previous literature for other engineering alloys [34].

The average electrical conductivity, measured using the Four-Point Direct-Current Potential Drop Measurements technique along the entire sample height, was found to be identical for both specimens (3.6 % IACS). This confirms that the difference between the processes did not affect this specific material property. Since both the electric and thermal conductivities depend on electron mobility, it is also expected that the hot forging arc-based AM variant also does not affect the material's thermal conductivity. Fig. 6 illustrates the evolution of electrical conductivity along the sample height. Moreover, measurements showed a standard deviation of 2.7 % and 2.4 % for CO and HF samples, respectively. This low deviation suggests high material homogeneity within each sample, a characteristic which will be later confirmed by microhardness evaluation along the vertical direction of the cross section. The correlation between electrical conductivity and hardness patterns is well-established, as both measurements depend on the material's microstructure. [41].

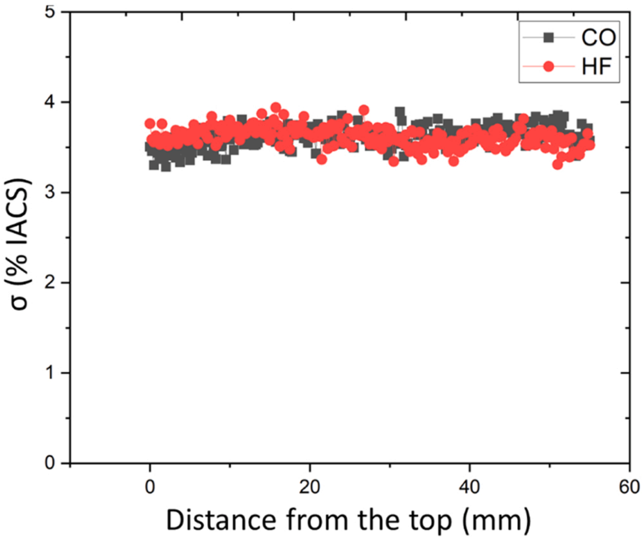

Fig. 6. Average electrical conductivity measured by the four-point potential drop technique along the sample height.

3.1. Microstructural characterization

Fig. 7a-b depicts the macrostructure evaluation of the CO and HF wall cross sections samples, respectively. Large columnar grains oriented towards the Z axis are evident in Fig. 7a, these grain structures are

Fig. 7. Optical macrography of the CO and HF wall cross sections samples.

characteristic of WAAM parts and are associated to directional heat extraction during additive manufacturing. The presence of columnar grains can lead to an anisotropic behavior in terms of mechanical, electrical, and thermal properties [49]. This negative effect was successfully reduced by the hot forging process, as observed in Fig. 8b. Although the reduction of the grain size could be qualitative, columnar grains were still observed in the microstructure. High strength in WAAM-fabricated materials is attributed to a fine microstructure, a high density of dislocations, and low-angle grain boundaries [50]. In this context, higher grain boundary density could be observed in the HF sample (Fig. 8b) when compared to the CO (Fig. 8a) condition. Moreover, the effect of dynamic recrystallization is also noted, as evidenced by the presence of new, smaller grains, resulting in a more refined grain structure. This increment in grain boundary density, and consequently higher expected dislocation density, suggests an overall improvement in mechanical strength in the HF wall when compared with CO wall. Finally, in Fig. 9a-b it is also noted the differences in dendrite orientation and microstructure morphology across the fusion layer. In Fig. 9a, the microstructure before the fusion layer reveals a coarse dendrite morphology when compared to the microstructure after the fusion line, which can also be observed in Fig. 9b. This effect may have been caused by the heat cycles created by post layers depositions. Although this effect is visible in the 2 walls, the HF (Fig. 9b) reveals a more significant microstructure refinement and a different dendrite orientation when compared with the region after the fusion line.

To quantitatively investigate the microstructure of the fabricated Ni-based superalloys, EBSD analysis was conducted at three distinct positions on the material’s cross sections: bottom, middle and top. The EBSD data confirms a reduction in the average grain size in the top and middle regions of the HF specimen compared to the same regions of the CO specimen (1746 vs 1262 µm and 1053 vs 696 µm respectively), representing a percentual reduction of approximately 28 % and 34 %, respectively. No reduction in grain size for the HF sample compared to the CO was observed on the bottom region of the walls. During the first deposited layers, the molten pool exhibits a reduced length owing to higher cooling rates and lower heat accumulation compared to upper deposited layers. Consequently, it is hypothesized that, particularly in the HF-WAAM process, the hammer impacts the material in a region of lower temperature where the hot forging effectiveness diminishes, thereby elucidating the absence of significant changes observed in the material’s microstructure. Fig. 10 (left) and Fig. 11 (left) depict the EBSD images of the bottom, middle, and top regions of the CO and HF wall samples, respectively. Although columnar grains are observed in both samples, it is evident that the microstructure is more refined in the HF sample. This refinement is attributed to plastic deformation and recrystallization induced by the hot forging process, which reduces the length of these columnar grains effectively reducing the material texture. Once more, it is anticipated that this microstructural characteristic can contribute to enhance the strength and more isotropic

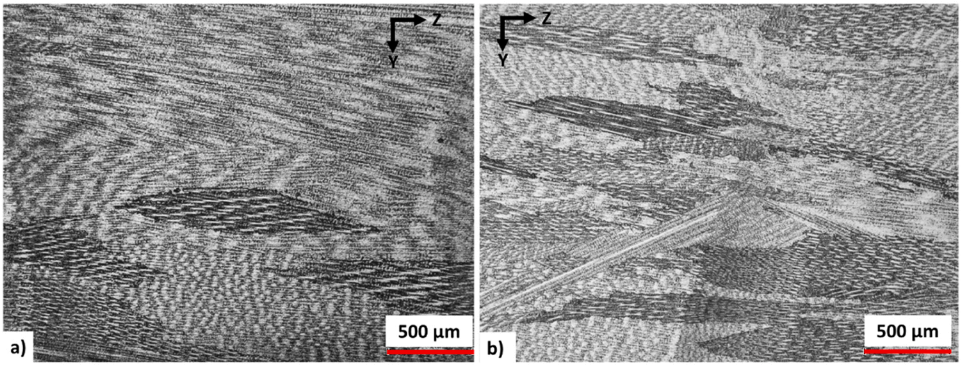

Fig. 8. Optical microscopy of CO (left) and HF (right) samples, highlighting the differences in grain boundary density.

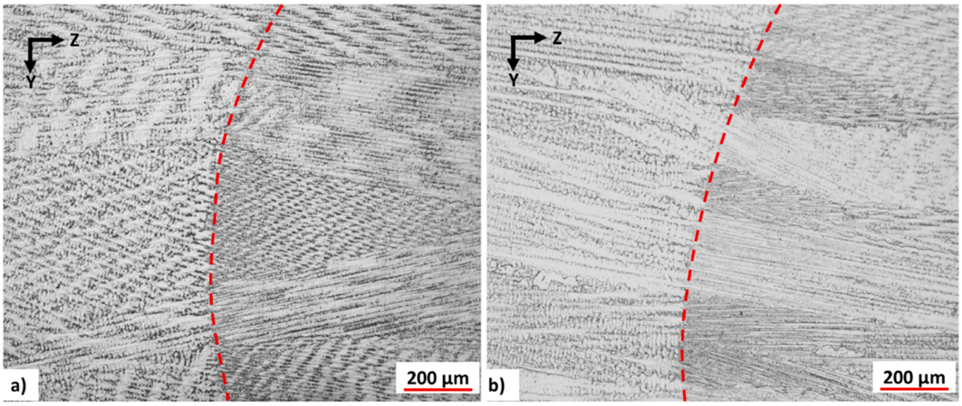

Fig. 9. Differences in dendrite orientation and microstructure morphology across the fusion layer: CO sample (left) and HF sample (right). The red dashed line details the fusion boundary between consecutively deposited layers.

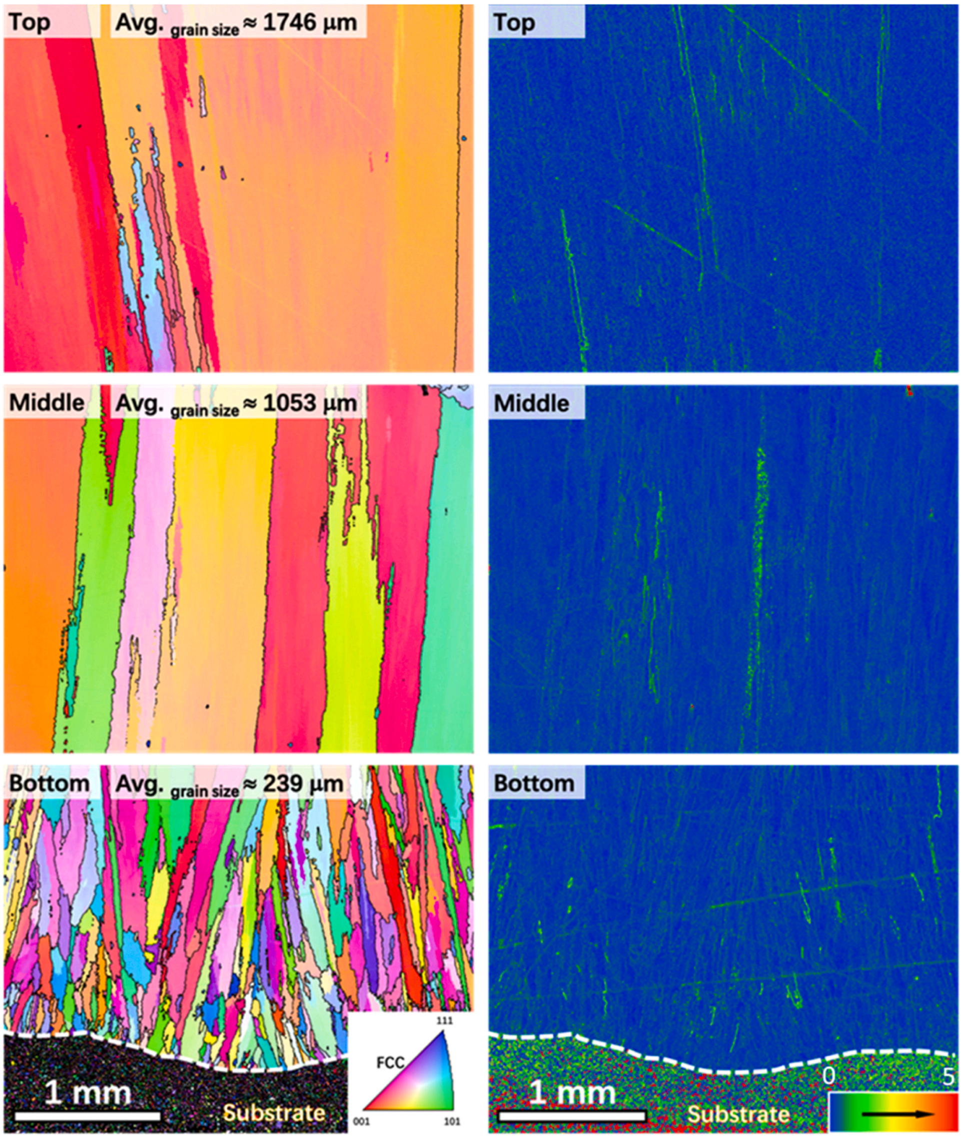

Fig. 10. Orientation image maps (left) obtained from EBSD analysis of Ni-based superalloy Haynes®282 of top, middle and bottom regions of the CO sample. On the right, kernel average misorientation (KAM) maps of the same regions.

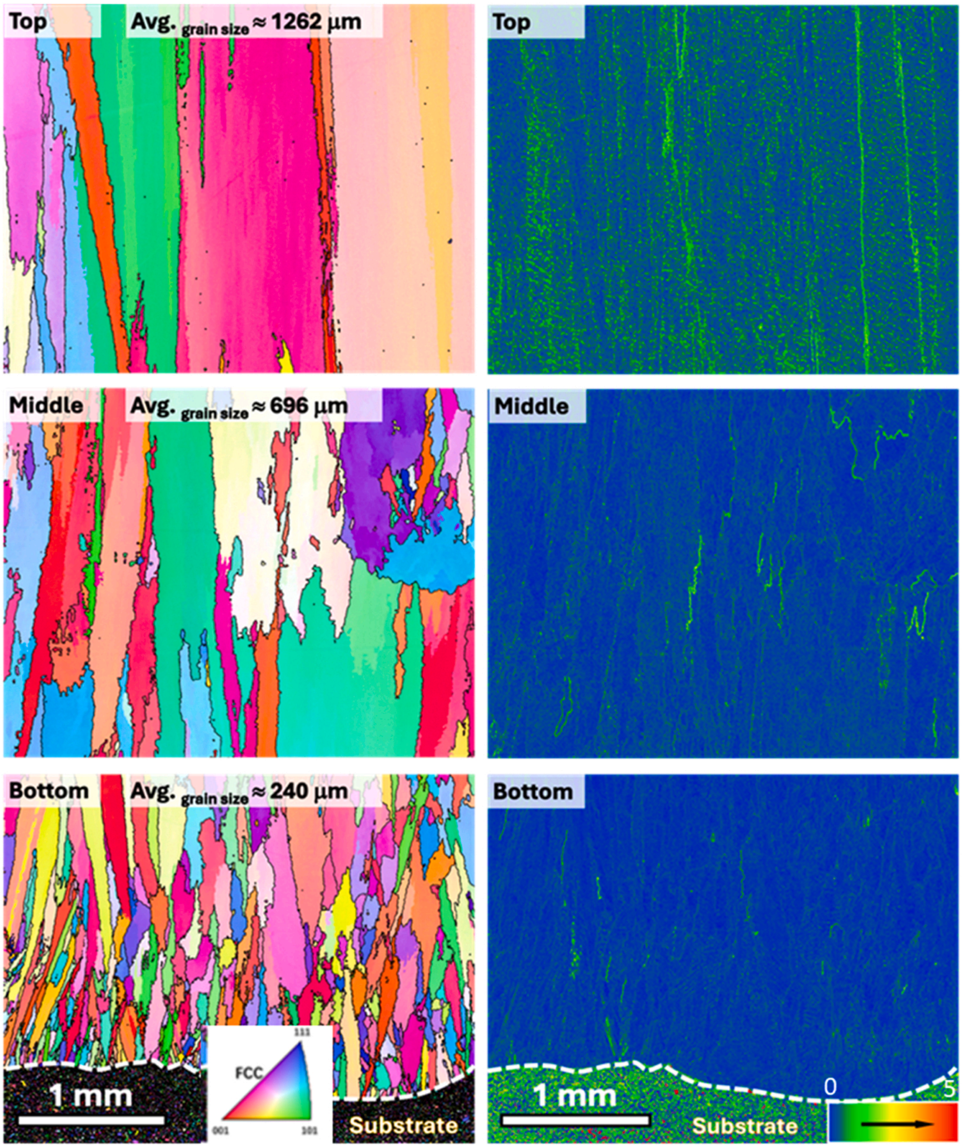

Fig. 11. Orientation image maps (left) obtained from EBSD analysis of Ni-based superalloy Haynes®282 of top, middle and bottom regions of the HF sample. On the right, kernel average misorientation (KAM) maps of the same regions.

mechanical response. The microstructure near the substrate tends to be more refined primarily due to steep thermal gradients — resulting from the heat deposited onto the cooler substrate — higher cooling rates owing to direct contact with the substrate, efficient heat dissipation facilitated by the substrate's high thermal conductivity acting as a heat sink, and metallurgical factors. The substrate and initial layers serve as effective nucleation sites for grain formation due to their relatively lower temperatures and existing grain structures, characteristics inherent to the process [51,52]. Ultimately, the average grain size in the lower region of both walls was significantly smaller compared to other regions, with no distinguishable difference between the HF and CO walls in this specific area. In this study, as the interaction between the substrate and deposited material was not evaluated, this region holds lesser significance compared to others. Nevertheless, analyses pertaining to substrate composition, preheating application, and other pertinent factors must be addressed.

During hot forging, the material is subjected to high temperatures and pressures, leading to dynamic recrystallization. This process continuously replaces deformed grains with new, smaller grains during the deformation itself, resulting in a fine-grained microstructure. The high temperature facilitates atomic movement, promoting the nucleation and growth of new grains [53,54]. As seen in Fig. 10 and Fig. 11, the hot forging process promoted the expected new nucleation sites, as a clear reduction of the average grain size was observed. A slight difference is observed for Kernel Average Misorientation (KAM), which is a quantitative measure used to analyze the local deformation or misorientation within polycrystalline materials. High KAM values typically indicate regions of high local deformation or strain, while low KAM values suggest regions with minimal deformation. In this regard, as expected by the deformation process, a frequency increase in higher angles KAM values was observed in the HF sample (Fig. 11 - right), while values closer to 0 were observed more frequently in the CO sample (Fig. 10 - right).

When grains exhibit preferred orientations, it results in anisotropy in the mechanical, physical, and chemical properties of materials. Therefore, measuring grain orientations in polycrystalline materials using EBSD data is a significant milestone in the development of crystallographic characterization techniques. Polar maps of CO and HF samples (Fig. 12 and Fig. 13, respectively) were generated to extract information regarding the orientations of the grains along the < 001 > , < 111 > , and < 101 > directions. Overall observation revealed a significantly higher texture intensity in the < 001 > orientation compared to

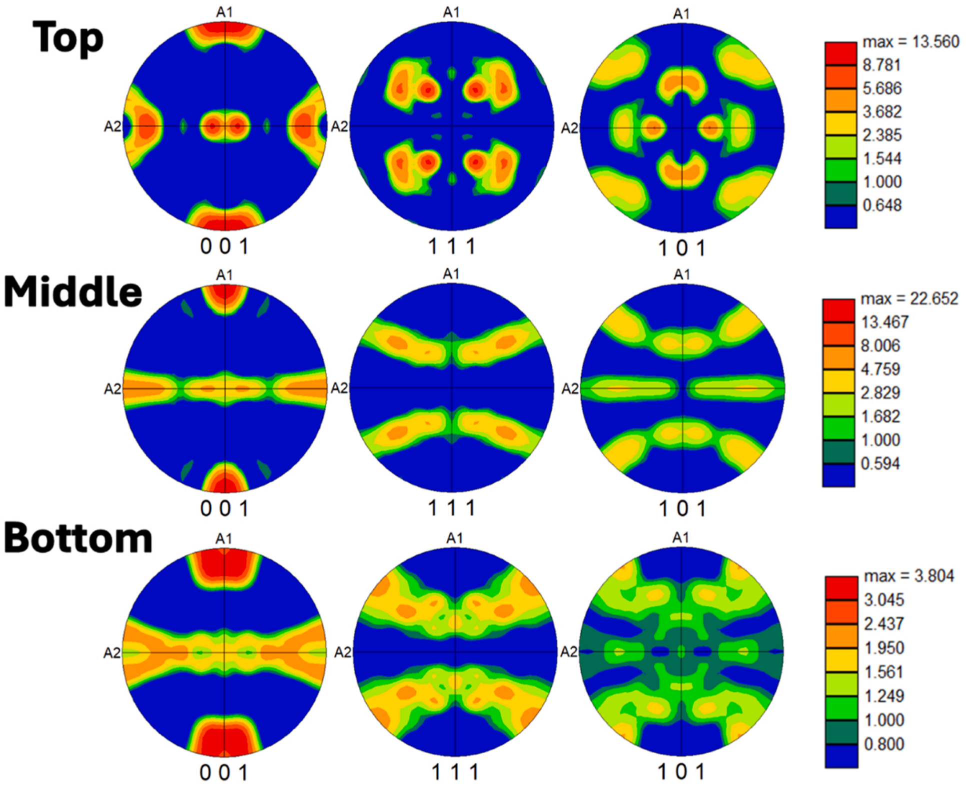

Fig. 12. Pole figures of top, middle and bottom regions of the CO sample fabricated via DED-AM.

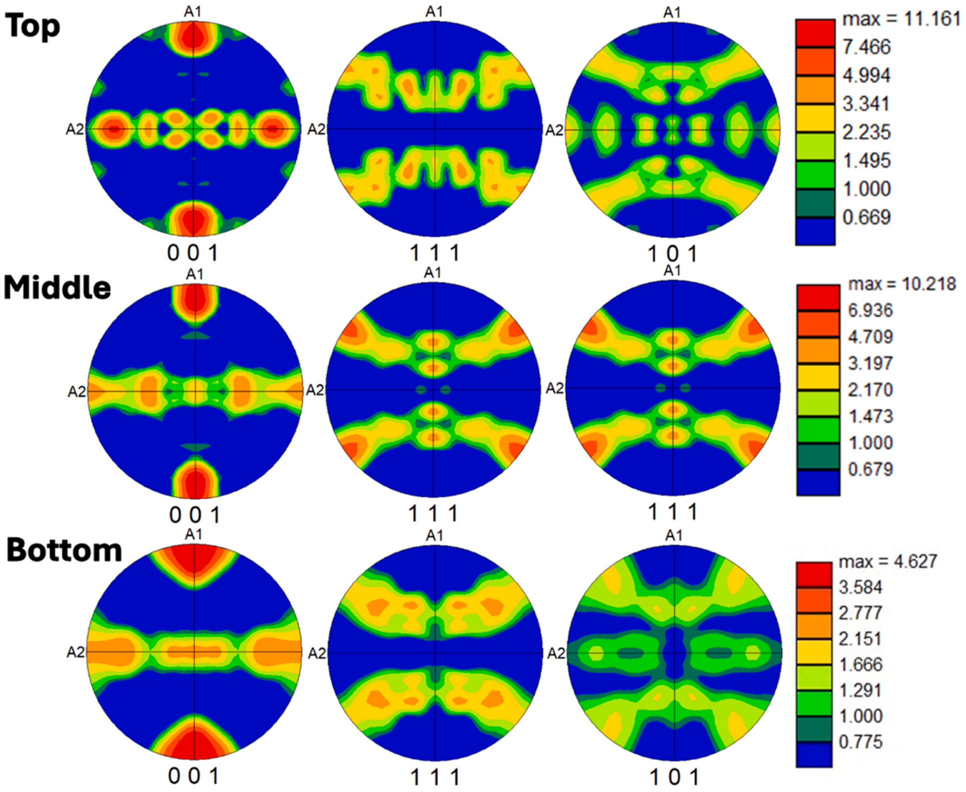

Fig. 13. Pole figures of top, middle and bottom regions of the HF sample fabricated via DED-AM.

< 111 > and < 101 > orientations at all three different positions. This orientation preference aligns with the growth direction of face-centered cubic materials [55]. During the layer-by-layer deposition process, the highly directional temperature gradient and thermal flux collectively contributed to the generation of this preferred orientation, thus promoting texture anisotropy. Similar phenomena have been widely

reported in other Ni-based alloys prepared by fusion-based additive manufacturing processes [56]. Comparing the texture intensities of grains along the < 001 > orientation at these three different positions, it was found that the grains in the middle regions exhibited the highest texture intensity, while those at the bottom exhibited the lowest (22.652 (middle) > 13.560 (top) > 3.804 (bottom)). This is primarily attributed to the presence of more random grains growing from newly nucleated grains in the lower regions [57]. Considering the HF sample, it can be observed that it exhibits a microstructure with lower pronounced crystal orientation. The lower texture index is associated with the formation of recrystallized and equiaxed grains within the fusion line, as well as thinner aligned grains. Therefore, considering the overall maintenance of columnar and cubic texture aspects, it can be inferred that the HF-WAAM process has a slight influence on solidification conditions. However, both conditions exhibit typical fusion-based crystal structures (cubic components, (<100 > {100}) [58].

Synchrotron X-ray diffractograms and 2D Debye-Scherrer rings were used to evaluate the differences in phase composition, volume fractions and texture of the as-deposited materials obtained by both processes. The observed diffraction rings of CO and HF samples (Fig. 14, left and right respectively) present patchy and discontinuous characteristics, which is a suggestion of oriented microstructure and coarse grains. The less intense features on the HF sample indicates a finer and less oriented microstructure, in accordance with the EBSD analysis (Figs. 10, 11, 12 and 13). The diffraction patterns were further processed and presented in Fig. 15 after full integration of the 2D Debye-Scherrer rings along the azimuthal angle. Similar diffraction patterns were observed for the samples, including the phase composition. The low fraction of precipitates of the as-built material emphasizes the essentiality of applying post-deposition heat treatments (PDHTs) to improve the microstructural characteristics and consequently the mechanical properties. Pizano et al. and Zhang et al. [39,40,59] used different combinations and temperatures for HIP, solution and aging heat treatments to promote an increase in strength by changing the MC- and $M_{23}C_6$-type carbides and others γ' precipitates growth, and enhancing the microstructural heterogeneity, in terms of texture and grain size. As this work aimed to evaluate the effects of in-situ hot forging during arc-based additive manufacturing on the deposited material, PDHTs were not applied. However, it is crucial to highlight that heat treatments optimization is imperative to improve the mechanical properties of superalloys prepared by additive manufacturing [39]. As also reported by Farias et al. [32], σ and η phases have not been observed. In this study, it was suggested that while these phases are thermodynamically predicted under a solid/liquid local equilibrium condition (using the Scheil-Gulliver model), the thermal conditions, specifically the rapid cooling rate during DED processes, inhibit their formation. The main differences observed were associated with peak intensity, wherein the HF sample exhibited (111), (200), and (220) diffraction peaks of higher intensity (indicating lower orientation) compared to the CO sample.

Despite the homogeneous composition of the bulk deposited metal, dendritic structures were observed, and this morphology typically exhibit microsegregation due to non-equilibrium solidification. This phenomenon, commonly encountered in solidified structures such as castings and welds, leads to chemical inhomogeneity, which can adversely affect mechanical properties [60,61]. The formation of the Laves phase, a result of segregation, is particularly significant in nickel-based superalloys used in aerospace applications. This phase can compromise structural integrity, potentially leading to premature failure of critical components during service, with serious implications for safety and financial cost[61]. Also, it is well established that Ni-based superalloys containing Nb and Fe can form the metastable γ'' phase [62]. Additionally, most γ''-containing alloys include elements like Al and Ti. Although the Haynes 282 alloy lacks Nb in its chemical composition, other elements such as molybdenum, silicon, iron, aluminum, and titanium can lead to significant enrichment of the interdendritic regions, resulting in segregation [61]. Consequently, it is crucial to consider that phases such as Laves and γ'' may constitute a minor yet significant portion of the microstructure of this superalloy under investigation.

Fig. 16 presents the heatmap of hardness measurements for CO and HF samples, with values ranging from 250 HV to 325 HV for both walls. According to the theory of mechanical hardening for hot forging processes, an increase in hardness is expected for the forged material. This is attributed to the plastic deformation experienced during forging, which introduces dislocations into the metal crystal structure. Theoretically, these dislocations impede the movement of other dislocations, enhancing resistance to further deformation and resulting in strain hardening, which increases the metal's hardness and strength. [63].

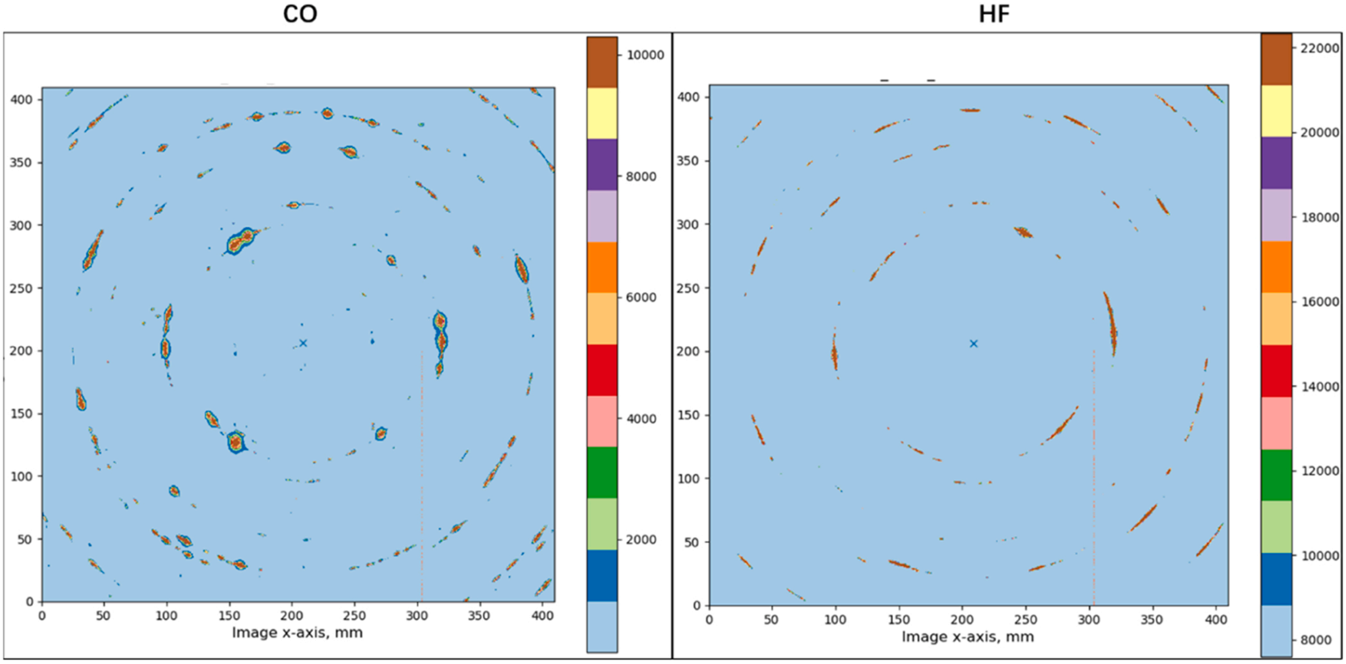

Fig. 14. 2D Debbye-Scherrer diffractions rings of the CO (left) and HF (right) Haynes®282 samples.

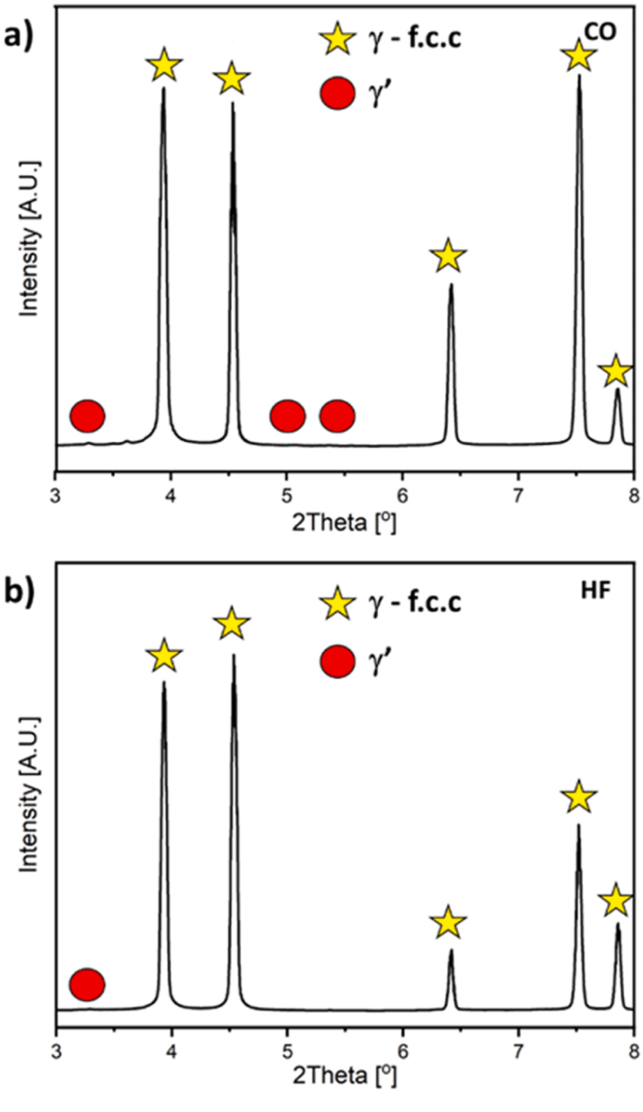

Fig. 15. Synchrotron X-ray diffractograms of the CO (top) and HF (bottom) as-built samples.

However, the analysis revealed no significant difference in hardness between the two samples, with only a 1.1 % increase for material in which the HF process was used. The average hardness values for CO and HF samples were 282.3 ± 3.1 HV and 285.4 ± 2.8 HV, respectively, indicating a negligible variation in hardness between the processes. Additionally, the percentage standard deviations of average hardness were low for both processes (1.1 % for CO and 1.0 % for HF), confirming the uniformity of the deposited material as previously verified by conductivity measurements. In nickel-based superalloys, material strengthening is more significantly influenced by solid solution effects than by grain size, as described by the Hall-Petch relationship. Solid solution strengthening occurs when atoms of different elements are added to the metal matrix, creating lattice distortions due to the size mismatch between the solute atoms and the host metal atoms. These distortions impede dislocation motion, which is critical in plastic deformation. In high-temperature applications, the effectiveness of grain size strengthening is further diminished due to grain growth or recrystallization [64–66].

3.2. Mechanical characterization

The tensile specimens retrieved in both vertical and horizontal orientations were tested at room temperature and the resulting stress-strain

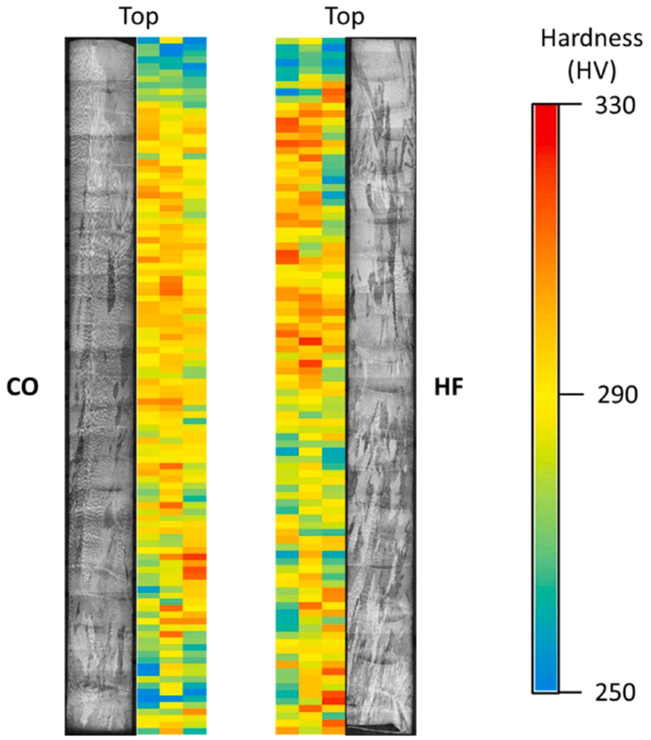

Fig. 16. Vickers microhardness (HV0.5) of the HF and CO cross sectional samples.

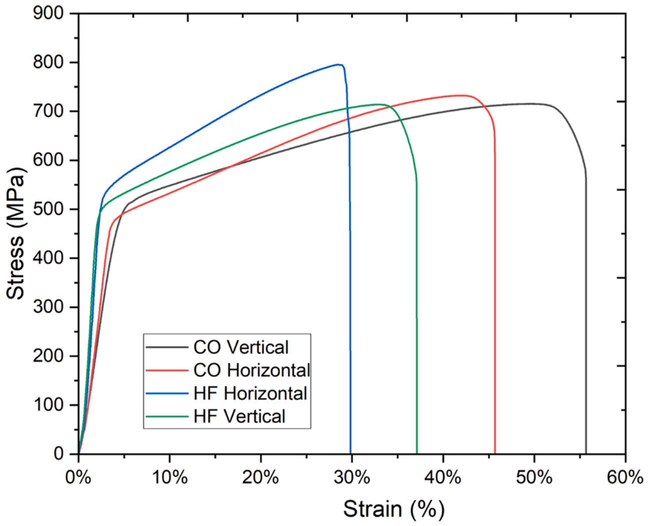

Fig. 17. Uniaxial tensile test of the Haynes®282 on vertical and horizontal directions for HF and CO walls.

Table 3
Values of UTS, 0.2 % (OYS) and E for Haynes®282 CO and HF specimen on vertical and horizontal directions.

	UTS (MPa)	0.2 % OYS (MPa)	Elongation (%)
CO Vertical	715	443	56 %
CO Horizontal	732	453	46 %
HF Vertical	714	485	38 %
HF Horizontal	795	522	32 %

curves are depicted in Fig. 17. Values of ultimate tensile strength (UTS), 0.2 % offset yield strength (OYS) and elongation (E) are presented in Table 3. No significant difference (less than 2.5 %) between vertical and horizontal directions was observed for UTS and 0.2 % OYS values on CO wall tensile samples. Nevertheless, the elongation in the vertical direction was higher (56 % vs 46 % in the horizontal direction), possibly attributable to the alignment of the material's microstructure. In arc-based additive manufacturing processes, the microstructure of the deposited material tends to align more favorably in the vertical direction due to the layering process and heat flow. This alignment can result in improved elongation characteristics along the vertical axis. The ultimate tensile strength (UTS) and 0.2 % offset yield strength (0.2 % OYS) of HF tensile samples exhibited similar trends to the CO ones. However, the variation from horizontal to vertical orientation was more pronounced (11 % for UTS and 7.5 % for 0.2 % OYS) in the forged material. In this study, the hot forging promoted an increase in grain boundary density, however grains remained with a columnar morphology. Consequently, the increase of strength (especially UTS) was observed for samples on the horizontal direction under load, as defects propagation encountered more boundaries (or barriers) during the movement along this specific orientation. Hot forging led to a noticeable reduction in elongation when comparing HF to CO samples. This decrease can be attributed to the effects of dynamic recrystallization, which results in grain refinement and the formation of a directional texture. Additionally, the redistribution of residual stresses and the increased dislocation density caused by strain hardening contribute to improved strength but limit the material's ability to undergo plastic deformation. Moreover, the presence of microdefects, such as hot and cold cracks, non-metallic inclusions, segregation of alloying elements, impurities, and secondary phases, further reduces elongation. These defects hinder the material's plastic deformation capability, act as initiation points for cracks, and lead to localized embrittlement and grain boundary weakening, ultimately compromising ductility. The mechanical properties of nickel-based superalloys are influenced by grain size, strengthening phases, dislocation density, recrystallization, texture, element segregation, secondary phases, and carbide morphology. Refined grains, controlled precipitation, and fine carbides enhance strength and ductility, while coarse grains, uneven precipitates, residual dislocations, partial recrystallization, and brittle phases reduce elongation and toughness.

As previously mentioned, it is expected that the forging process promotes a grain size reduction which increases the amount of grain boundaries that difficult dislocation slips and increase the material strength. According to the Hall-Petch equation, smaller grain size translates into higher mechanical strength [34]. When comparing overall results between HF and CO samples, this effect was only significantly effective for the HF sample obtained on the horizontal direction because not fully equiaxed grains were obtained in the HF produced microstructure, as previously observed in Fig. 10 and Fig. 11. If a more intense grain refinement was observed, with equiaxed grains formation, an increase of strength in both horizontal and vertical directions would be expected. Despite lower elongation, hot forged materials often exhibit superior mechanical performance, in terms of ultimate tensile strength, which makes them desirable for applications where these properties are critical, such as aerospace components, automotive parts, and high-performance machinery. It is worth noting that the HF process altered the 0.2 % offset yield strength (OYS) even without changes in hardness. This result confirms that, for this material, solid solution strengthening is the primary mechanism for material strengthening. Additionally, hot forging in a nickel-based superalloy predominantly affects its microstructure, such as grain refinement or texture changes, which can enhance the yield strength without significantly impacting the hardness. Fig. 18 depicts the fracture surfaces of horizontal samples after the tensile test, which presented a ductile aspect, mainly composed of dimples. No significant differences were observed between the CO and HF specimens, which can be attributed to the minimal variation in phase composition and volume fractions resulting from the hot forging process. Furthermore, due to the position where secondary phases are generally nucleated in nickel-based super alloys, the dendritic morphology was still found on the fractographies [67,68].

4. Conclusions

In this study, the effects of hot forging on the arc-based additive manufacturing of Haynes®282, a nickel-based superalloy, were evaluated in terms of microstructure and mechanical behavior. Thermal control during deposition was managed using interpass time, and a high-

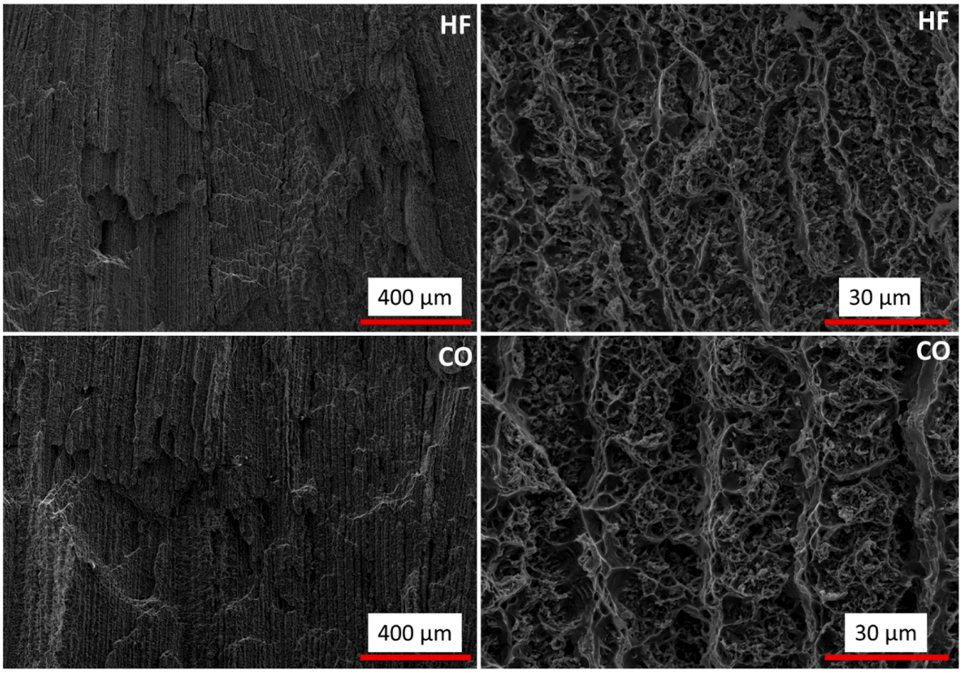

Fig. 18. Fracture surfaces of the CO and HF horizontal tensile samples after the test.

speed camera was employed to measure the molten pool dimensions, which facilitated the calculation of the optimal hammer size. Two single-bead multi-layered walls were fabricated: one with hot forging and one without. The instantaneous impact forging force was determined to be 1022 N, leading to a 22 % reduction in volume of voids. Both walls exhibited similar electrical conductivity and hardness levels, with the forged sample showing a discrete increase of 1.1 % in hardness. The microstructure of the forged material displayed a higher grain boundary density and a lower average grain size, with reductions of 34 % in the middle regions and 28 % in the top regions compared to the non-forged material. The hot forged microstructure was finer and less oriented, as confirmed by synchrotron X-ray diffraction rings, indicating successful grain refinement. Both walls exhibited the same phases, mainly γ – fcc and γ' phases. The forged sample in the horizontal direction presented increased ultimate tensile strength (UTS), highlighting the impact of grain refinement. As expected, elongation was reduced in the hot forged material. This study marks the first application of hot forging for Haynes®282 in arc-based additive manufacturing and demonstrates its effectiveness. Further process optimization and thermal monitoring improvements could enhance deformation efficiency, leading to better grain refinement and mechanical performance.

CRediT authorship contribution statement

Gomes dos Santos Telmo: Writing – review & editing, Visualization, Supervision, Resources, Project administration, Methodology, Investigation, Funding acquisition, Formal analysis, Data curation, Conceptualization. **Schell Norbert:** Resources, Investigation. **Xiong Wei:** Writing – review & editing, Investigation, Data curation. **Ladinos Pizano Luis Fernando:** Writing – review & editing, Investigation, Data curation. **Shen Jiajia:** Writing – review & editing, Writing – original draft, Investigation, Formal analysis, Data curation. **Rodrigues Marçal Pedro:** Writing – original draft, Investigation, Formal analysis, Data curation. **Oliveira Felice Igor:** Writing – original draft, Validation, Methodology, Investigation, Formal analysis, Data curation, Conceptualization. **Oliveira João Pedro:** Writing – review & editing, Visualization, Supervision, Resources, Project administration, Methodology, Investigation, Funding acquisition, Formal analysis, Data curation, Conceptualization.

Declaration of Competing Interest

The authors declare that they have no known competing financial interests or personal relationships that could have appeared to influence the work reported in this paper.

Acknowledgements

The authors acknowledge Fundação para a Ciência e a Tecnologia (FCT, I.P.) for its financial support via the project UIDB/00667/2020 and UIDP/00667/2020 (UNIDEMI). JPO acknowledges funding by national funds from FCT - Fundação para a Ciência e a Tecnologia, I.P., in the scope of the projects LA/P/0037/2020, UIDP/50025/2020 and UIDB/50025/2020 of the Associate Laboratory Institute of Nanostructures, Nanomodelling and Nanofabrication – i3N. IOF acknowledges Fundação para a Ciência e a Tecnologia (FCT, I.P.), Portugal, for funding the Ph.D. Grant 2023.03610.BD. JS acknowledges the China Scholarship Council for funding the Ph.D. grant (CSC NO. 201808320394). This activity has received funding from the European Institute of Innovation and Technology (EIT) – Project Smart WAAM: Microstructural Engineering and Integrated Non-Destructive Testing. This body of the European Union receives support from the European Union's Horizon 2020 Research and Innovation Programme.

Data availability

Data will be made available on request.

References

[1] I.O. Felice, J. Shen, A.F.C. Barragan, I.A.B. Moura, B. Li, B. Wang, H. Khodaverdi, M. Mohri, N. Schell, E. Ghafoori, T.G. Santos, J.P. Oliveira, Wire and arc additive manufacturing of Fe-based shape memory alloys: microstructure, mechanical and functional behavior, Mater. Des. 231 (2023) 112004, https://doi.org/10.1016/j.matdes.2023.112004.

[2] V.A. Wankhede, S. Vinodh, Analysis of challenges of wire-arc additive manufacturing process in the context of Industry 4.0 using graph theory approach, Int. J. Adv. Manuf. Technol. 123 (2022) 1059–1078, https://doi.org/10.1007/s00170-022-10233-z.

[3] S. Chauhan, A. Narasimhulu, Comprehensive Study on Wire Arc Additive Manufacturing (WAAM) (2024) 281–305, https://doi.org/10.1007/978-981-99-5613-5_22.

[4] M. Navarro, A. Matar, S.F. Diltemiz, M. Eshraghi, Development of a low-cost wire arc additive manufacturing system, J. Manuf. Mater. Process. 6 (2021) 3, https://doi.org/10.3390/jmmp6010003.

[5] M. Lalegani Dezaki, A. Serjouei, A. Zolfagharian, M. Fotouhi, M. Moradi, M.K. A. Ariffin, M. Bodaghi, A review on additive/subtractive hybrid manufacturing of directed energy deposition (DED) process, Adv. Powder Mater. 1 (2022) 100054, https://doi.org/10.1016/j.apmate.2022.100054.

[6] L.J. da Silva, D.M. Souza, D.B. de Araújo, R.P. Reis, A. Scotti, Concept and validation of an active cooling technique to mitigate heat accumulation in WAAM, Int. J. Adv. Manuf. Technol. 107 (2020) 2513–2523, https://doi.org/10.1007/s00170-020-05201-4.

[7] V. Dimatteo, E. Liverani, A. Ascari, A. Fortunato, Weldability and mechanical properties of dissimilar laser welded aluminum alloys thin sheets produced by conventional rolling and Additive Manufacturing, J. Mater. Process Technol. 302 (2022) 117512, https://doi.org/10.1016/j.jmatprotec.2022.117512.

[8] B.K. Nagesha, V. Dhinakaran, M. Varsha Shree, K.P. Manoj Kumar, T. Jagadeesha, A review on weldability of additive manufactured titanium alloys, Mater. Today Proc. 33 (2020) 2964–2969, https://doi.org/10.1016/j.matpr.2020.02.899.

[9] V.-P. Matilainen, J. Pekkarinen, A. Salminen, Weldability of additive manufactured stainless steel, Phys. Procedia 83 (2016) 808–817, https://doi.org/10.1016/j.phpro.2016.08.083.

[10] N. Solanke, R.M. Metkar, Optimization of welding process parameters of wire arc additive manufacturing, J. Phys. Conf. Ser. 2763 (2024) 012018, https://doi.org/10.1088/1742-6596/2763/1/012018.

[11] K. Marumoto, A. Fujinaga, T. Takahashi, H. Yamamoto, M. Yamamoto, Selection of welding conditions for achieving both a high efficiency and low heat input for hot-wire gas metal arc welding, J. Manuf. Mater. Process. 8 (2024) 82, https://doi.org/10.3390/jmmp8020082.

[12] M. Karmuhilan, S. Kumanan, Effect of inter-pass layer temperatures on microstructure and mechanical properties of Inconel 625 fabricated using wire and arc additive manufacturing, J. Mater. Eng. Perform. (2024), https://doi.org/10.1007/s11665-024-09148-5.

[13] N.L. Piercy, J.D. Kulkarni, A.S. Vishnu, S. Suryakumar, K.D. Cole, P.K. Rao, Rapid thermal modeling of wire arc additive manufacturing process using a mesh-free spectral graph theory approach, Int. J. Adv. Manuf. Technol. (2024), https://doi.org/10.1007/s00170-024-13994-x.

[14] I. Mishra, R. Srivastava, Thermal simulation of Al alloy developed by wire arc additive manufacturing using finite element analysis, Int. J. Interact. Des. Manuf. (IJIDeM (2024), https://doi.org/10.1007/s12008-024-01973-1.

[15] M.S. Kumar, C.-H. Yang, V. Aravinthan, A.A. Adediran, S.R. Begum, M. Vasumathi, T.C. Jen, Influence of low heat input by CMT powered WAAM on attaining the microstructural and mechanical homogeneity of printed 304 SS cylindrical component, Results Eng. 21 (2024) 101846, https://doi.org/10.1016/j.rineng.2024.101846.

[16] A.K. Maurya, J.-T. Yeom, J.H. Kim, C.H. Park, J.-K. Hong, J.-H. Yang, N.H. Kang, S. Cheon, N.S. Reddy, M. Cheepu, S.-M. Cho, Wire Arc Additive manufacturing method for Ti-6Al-4V alloy to improve the grain refinement efficiency and mechanical properties, J. Mater. Res. Technol. (2024), https://doi.org/10.1016/j.jmrt.2024.06.240.

[17] J. Donoghue, A.A. Antonysamy, F. Martina, P.A. Colegrove, S.W. Williams, P. B. Prangnell, The effectiveness of combining rolling deformation with Wire–Arc Additive Manufacture on β-grain refinement and texture modification in Ti–6Al–4V, Mater. Charact. 114 (2016) 103–114, https://doi.org/10.1016/j.matchar.2016.02.001.

[18] A.R. McAndrew, M. Alvarez Rosales, P.A. Colegrove, J.R. Hönnige, A. Ho, R. Fayolle, K. Eyitayo, I. Stan, P. Sukrongpang, A. Crochemore, Z. Pinter, Interpass rolling of Ti-6Al-4V wire + arc additively manufactured features for microstructural refinement, Addit. Manuf. 21 (2018) 340–349, https://doi.org/10.1016/j.addma.2018.03.006.

[19] G. Marinelli, F. Martina, S. Ganguly, S. Williams, Grain refinement in an unalloyed tantalum structure by combining Wire+Arc additive manufacturing and vertical cold rolling, Addit. Manuf. 32 (2020) 101009, https://doi.org/10.1016/j.addma.2019.101009.

[20] L. Neto, S. Williams, J. Ding, J. Hönnige, F. Martina, Mechanical Properties Enhancement of Additive Manufactured Ti-6Al-4V by Machine Hammer Peening (2020) 121–132, https://doi.org/10.1007/978-981-15-0054-1_13.

[21] J.R. Hönnige, A.E. Davis, A. Ho, J.R. Kennedy, L. Neto, P. Prangnell, S. Williams, The effectiveness of grain refinement by machine hammer peening in high deposition rate wire-arc AM Ti-6Al-4V, Metall. Mater. Trans. A 51 (2020) 3692–3703, https://doi.org/10.1007/s11661-020-05781-6.

[22] C. Wang, Y. Li, W. Tian, J. Hu, B. Li, P. Li, W. Liao, Influence of ultrasonic impact treatment and working current on microstructure and mechanical properties of 2219 aluminium alloy wire arc additive manufacturing parts, J. Mater. Res. Technol. 21 (2022) 781–797, https://doi.org/10.1016/j.jmrt.2022.09.055.

[23] Y. Chen, M. Xu, T. Zhang, J. Xie, K. Wei, S. Wang, L. Yin, P. He, Grain refinement and mechanical properties improvement of Inconel 625 alloy fabricated by ultrasonic-assisted wire and arc additive manufacturing, J. Alloy. Compd. 910 (2022) 164957, https://doi.org/10.1016/j.jallcom.2022.164957.

[24] M. Diao, C. Guo, Q. Sun, F. Jiang, L. Li, J. Li, D. Xu, C. Liu, H. Song, Improving mechanical properties of austenitic stainless steel by the grain refinement in wire and arc additive manufacturing assisted with ultrasonic impact treatment, Mater. Sci. Eng. A 857 (2022) 144044, https://doi.org/10.1016/j.msea.2022.144044.

[25] H. Su, B. Shao, J. Liu, Y. Zong, D. Shan, Effect of hot deformation on microstructure and porosity of additively manufactured 7050 Al alloy, Adv. Eng. Mater. 26 (2024), https://doi.org/10.1002/adem.202301124.

[26] J. Huang, Y. Fu, W. Zhai, R. Li, X. Zhao, H. Lin, H. Zhang, G. Wang, Hybrid interlayer hot rolling and wire arc additive manufacturing of Al-Mg alloy: microstructure, mechanical properties and strengthening mechanism, J. Mater. Res. Technol. 30 (2024) 7037–7050, https://doi.org/10.1016/j.jmrt.2024.05.085.

[27] Z. Xu, J. Xiao, S. Chen, A novel high-dynamic actuator based in-situ micro-forging process for wire arc additive manufacturing of aluminum alloy, J. Mater. Process Technol. 324 (2024) 118259, https://doi.org/10.1016/j.jmatprotec.2023.118259.

[28] C. Ma, Y. Liu, C. Li, H. Dong, D. Li, X. Wu, P. Liu, Q. Sun, H. Jin, F. Zhang, Mechanical properties of carbon steel by compound arc and vibration shock forging-rolling, J. Manuf. Process 60 (2020) 11–22, https://doi.org/10.1016/j.jmapro.2020.10.005.

[29] Y. Fu, M. Zhang, X. Chen, G. Wang, H. Zhang, Hot deformation behavior and process optimization of TC4-DT alloy fabricated by wire and arc additive manufacturing with in-situ forging, J. Mater. Res. Technol. 30 (2024) 5056–5068, https://doi.org/10.1016/j.jmrt.2024.04.226.

[30] A.K. Maurya, J.-T. Yeom, S.W. Kang, C.H. Park, J.-K. Hong, N.S. Reddy, Optimization of hybrid manufacturing process combining forging and wire-arc additive manufactured Ti-6Al-4V through hot deformation characterization, J. Alloy. Compd. 894 (2022) 162453, https://doi.org/10.1016/j.jallcom.2021.162453.

[31] V.R. Duarte, T.A. Rodrigues, N. Schell, R.M. Miranda, J.P. Oliveira, T.G. Santos, In-situ hot forging directed energy deposition-arc of CuAl8 alloy, Addit. Manuf. 55 (2022) 102847, https://doi.org/10.1016/j.addma.2022.102847.

[32] F.W.C. Farias, V.R. Duarte, I.O. Felice, J. da, C.P. Filho, N. Schell, E. Maawad, J. A. Avila, J.Y. Li, Y. Zhang, T.G. Santos, J.P. Oliveira, In situ interlayer hot forging arc-based directed energy deposition of Inconel® 625: process development and microstructure effects, Addit. Manuf. 66 (2023) 103476, https://doi.org/10.1016/j.addma.2023.103476.

[33] F.W.C. Farias, V.R. Duarte, J. da, C.P. Filho, A.R. Figueiredo, N. Schell, E. Maawad, J.Y. Li, Y. Zhang, M. Bordas-Czaplicki, F.M.A. da Fonseca, J. Cormier, T.G. Santos, J.P. Oliveira, High-performance Ni-based superalloy 718 fabricated via arc plasma directed energy deposition: effect of post-deposition heat treatments on microstructure and mechanical properties, Addit. Manuf. 88 (2024) 104252, https://doi.org/10.1016/j.addma.2024.104252.

[34] V.R. Duarte, T.A. Rodrigues, N. Schell, R.M. Miranda, J.P. Oliveira, T.G. Santos, Hot forging wire and arc additive manufacturing (HF-WAAM), Addit. Manuf. 35 (2020) 101193, https://doi.org/10.1016/j.addma.2020.101193.

[35] K.L. Kruger, HAYNES 282 alloy. in: Materials for Ultra-Supercritical and Advanced Ultra-Supercritical Power Plants, Elsevier, 2017, pp. 511–545, https://doi.org/10.1016/B978-0-08-100552-1.00015-4.

[36] M. Rowe, Ranking the resistance of wrought superalloys to strain-age cracking, Weld. J. 85 (2006) 7–34.

[37] J. Caron, Weldability and welding metallurgy of HAYNES 282 alloy, in: John Wiley & Sons (Ed.), International Symposium on Superalloy 718 and Derivatives, 2014: pp. 273–286.

[38] M. Rashid, S. Sabu, A. Kunjachan, M. Agilan, T. Anjilivelil, J. Joseph, Advances in wire-arc additive manufacturing of nickel-based superalloys: heat sources, DfAM principles, material evaluation, process parameters, defect management, corrosion evaluation and post-processing techniques, Int. J. Lightweight Mater. Manuf. (2024), https://doi.org/10.1016/j.ijlmm.2024.05.009.

[39] L.F.L. Pizano, S. Sridar, C. Sudbrack, W. Xiong, Microstructure Evolution During Post-heat Treatment of Haynes 282 Alloy Processed by Wire-Arc Additive Manufacturing, in: 2023: 773–788. https://doi.org/10.1007/978-3-031-27447-3_46.

[40] L.F.L. Pizano, S. Sridar, R.R. De Vecchis, X. Wang, J. Biddlecom, G.J. Pataky, C. Sudbrack, W. Xiong, Recrystallization behavior and mechanical properties of Haynes 282 fabricated by wire-arc additive manufacturing with post-heat treatment, J. Manuf. Process 119 (2024) 781–789, https://doi.org/10.1016/j.jmapro.2024.04.015.

[41] G.L. Sorger, J.P. Oliveira, P.L. Inácio, N. Enzinger, P. Vilaça, R.M. Miranda, T. G. Santos, Non-destructive microstructural analysis by electrical conductivity: comparison with hardness measurements in different materials, J. Mater. Sci. Technol. 35 (2019) 360–368, https://doi.org/10.1016/j.jmst.2018.09.047.

[42] A.B. Spierings, M. Schneider, R. Eggenberger, Comparison of density measurement techniques for additive manufactured metallic parts, Rapid Prototyp. J. 17 (2011) 380–386, https://doi.org/10.1108/13552541111156504.

[43] D.S.M. Serrati, M.A. Machado, J.P. Oliveira, T.G. Santos, Non-destructive testing inspection for metal components produced using wire and arc additive manufacturing, Metals 13 (2023) 648, https://doi.org/10.3390/met13040648.

[44] ISO, ISO 6507-1:2018(en) Metallic materials — Vickers hardness test — Part 1: Test method, 2018.

[45] L. Li, Y. Jiang, Y. Xiao, H. Chen, L. Shi, Numerical simulation of thermal processes in cold metal transfer-based additive manufacturing, Int. J. Adv. Manuf. Technol. 130 (2024) 4431–4442, https://doi.org/10.1007/s00170-024-13019-7.

[46] D.K. Gupta, R.S. Mulik, Numerical simulation and experimental investigation of temperature distribution during the wire arc additive manufacturing (WAAM) process, Prog. Addit. Manuf. (2024), https://doi.org/10.1007/s40964-024-00647-4.

[47] X. Zhou, Z. Fu, X. Zhou, X. Bai, Q. Tian, J. Fu, H. Zhang, Numerical simulation of heat and mass transient behavior during WAAM overlapping deposition with external deflection magnetic field, Int. J. Heat. Mass Transf. 218 (2024) 124780, https://doi.org/10.1016/j.ijheatmasstransfer.2023.124780.

[48] H. Mu, Z. Chen, F. He, Y. Li, C. Xia, P. Commins, Z. Pan, Defect Detection and Process Monitoring for Wire Arc Additive Manufacturing Using Machine Learning, in: 2022: pp. 3–22. https://doi.org/10.1007/978-981-19-3902-0_1.

[49] T. Zhang, H. Li, H. Gong, Y. Wu, X. Chen, X. Zhang, Study on location-related thermal cycles and microstructure variation of additively manufactured inconel 718, J. Mater. Res. Technol. 18 (2022) 3056–3072, https://doi.org/10.1016/j.jmrt.2022.03.178.

[50] X. Duan, X. Yang, Achieving enhanced strength and ductility in 316L stainless steel via wire arc additive manufacturing using pulsed arc plasma, Mater. Sci. Eng.: A 867 (2023) 144711, https://doi.org/10.1016/j.msea.2023.144711.

[51] T.A. Rodrigues, V. Duarte, R.M. Miranda, T.G. Santos, J.P. Oliveira, Current status and perspectives on wire and arc additive manufacturing (WAAM), Materials 12 (2019) 1121, https://doi.org/10.3390/ma12071121.

[52] A. Dash, L. Squires, J.D. Avila, S. Bose, A. Bandyopadhyay, Influence of active cooling on microstructure and mechanical properties of wire arc additively manufactured mild steel, Front. Mech. Eng. 9 (2023), https://doi.org/10.3389/fmech.2023.1130407.

[53] Z.X. Zhang, S.J. Qu, A.H. Feng, X. Hu, J. Shen, Microstructural mechanisms during multidirectional isothermal forging of as-cast Ti-6Al-4V alloy with an initial lamellar microstructure, J. Alloy. Compd. 773 (2019) 277–287, https://doi.org/10.1016/j.jallcom.2018.09.220.

[54] K. Zhu, S. Qu, A. Feng, J. Sun, J. Shen, Microstructural evolution and refinement mechanism of a beta–gamma TiAl-based alloy during multidirectional isothermal forging, Materials 12 (2019) 2496, https://doi.org/10.3390/ma12152496.

[55] Y. Wang, J. Shi, Texture control of Inconel 718 superalloy in laser additive manufacturing by an external magnetic field, J. Mater. Sci. 54 (2019) 9809–9823, https://doi.org/10.1007/s10853-019-03569-7.

[56] M. Ni, C. Chen, X. Wang, P. Wang, R. Li, X. Zhang, K. Zhou, Anisotropic tensile behavior of in situ precipitation strengthened Inconel 718 fabricated by additive manufacturing, Mater. Sci. Eng. A 701 (2017) 344–351, https://doi.org/10.1016/j.msea.2017.06.098.

[57] S. Paul, J. Liu, S.T. Strayer, Y. Zhao, S. Sridar, M.A. Klecka, W. Xiong, A.C. To, A discrete dendrite dynamics model for epitaxial columnar grain growth in metal additive manufacturing with application to Inconel, Addit. Manuf. 36 (2020) 101611, https://doi.org/10.1016/j.addma.2020.101611.

[58] X. Xu, S. Ganguly, J. Ding, C.E. Seow, S. Williams, Enhancing mechanical properties of wire + arc additively manufactured INCONEL 718 superalloy through in-process thermomechanical processing, Mater. Des. 160 (2018) 1042–1051, https://doi.org/10.1016/j.matdes.2018.10.038.

[59] H. Zhang, Y. Wang, R.R. De Vecchis, W. Xiong, Evolution of carbide precipitates in Haynes® 282 superalloy processed by wire arc additive manufacturing, J. Mater. Process Technol. 305 (2022) 117597, https://doi.org/10.1016/j.jmatprotec.2022.117597.

[60] Ch Radhakrishna, K.P. Rao, Studies on creep/stress rupture behaviour of superalloy 718 weldments used in gas turbine applications, Mater. High. Temp. 12 (1994) 323–327, https://doi.org/10.1080/09603409.1994.11752536.

[61] C. RADHAKRISHNA, K. PRASAD RAO, The formation and control of Laves phase in superalloy 718 welds, J. Mater. Sci. 32 (1997) 1977–1984, https://doi.org/10.1023/A:1018541915113.

[62] M.P. Haines, V.V. Rielli, S. Primig, N. Haghdadi, Powder bed fusion additive manufacturing of Ni-based superalloys: a review of the main microstructural constituents and characterization techniques, J. Mater. Sci. 57 (2022) 14135–14187, https://doi.org/10.1007/s10853-022-07501-4.

[63] G. Garcés, A. Müller, E. Oñorbe, P. Pérez, P. Adeva, Effect of hot forging on the microstructure and mechanical properties of Mg–Zn–Y alloy, J. Mater. Process Technol. 206 (2008) 99–105, https://doi.org/10.1016/j.jmatprotec.2007.12.014.

[64] W. Gao, J. Lu, J. Zhou, L. Liu, J. Wang, Y. Zhang, Z. Zhang, Effect of grain size on deformation and fracture of Inconel718: an in-situ SEM-EBSD-DIC investigation, Mater. Sci. Eng. A 861 (2022) 144361, https://doi.org/10.1016/j.msea.2022.144361.

[65] A. Lasalmonie, J.L. Strudel, Influence of grain size on the mechanical behaviour of some high strength materials, J. Mater. Sci. 21 (1986) 1837–1852, https://doi.org/10.1007/BF00547918.

[66] A. Heckl, S. Neumeier, M. Göken, R.F. Singer, The effect of Re and Ru on γ/γ' microstructure, γ-solid solution strengthening and creep strength in nickel-base

superalloys, Mater. Sci. Eng. A 528 (2011) 3435–3444, https://doi.org/10.1016/j.msea.2011.01.023.

[67] C.E. Seow, H.E. Coules, G. Wu, R.H.U. Khan, X. Xu, S. Williams, Wire + arc additively manufactured Inconel 718: effect of post-deposition heat treatments on microstructure and tensile properties, Mater. Des. 183 (2019) 108157, https://doi.org/10.1016/j.matdes.2019.108157.

[68] T. Zhang, H. Li, H. Gong, Y. Wu, A.S. Ahmad, X. Chen, Effect of rolling force on tensile properties of additively manufactured Inconel 718 at ambient and elevated temperatures, J. Alloy. Compd. 884 (2021) 161050, https://doi.org/10.1016/j.jallcom.2021.161050.